Evidence of Sea-State Dependence of Aerosol Concentration in the Marine Atmospheric Boundary Layer

LUC LENAIN AND W. KENDALL MELVILLE

Scripps Institution of Oceanography, La Jolla, California

(Manuscript received 11 March 2016, in final form 3 October 2016)

ABSTRACT

Sea spray aerosols represent a large fraction of the aerosols present in the maritime environment. Despite evidence of the importance of surface wave– and wave breaking–related processes in coupling the ocean with the atmosphere, sea spray source generation functions are traditionally parameterized by the 10-m wind speed U_{10} alone. It is clear that unless the wind and wave field are fully developed, the source function will be a function of both wind and wave parameters. This study reports primarily on the aerosol component of an air–sea interaction experiment, the phased-resolved High-Resolution Air–Sea Interaction Experiment (HIRES), conducted off the coast of northern California in June 2010. Detailed measurements of aerosol number concentration in the marine atmospheric boundary layer (MABL) at altitudes ranging from as low as 30 m up to 800 m above mean sea level (MSL) over a broad range of environmental conditions (significant wave height H_s of 2 to 4.5 m and U_{10} from 10 to 18 m s^{-1}) collected from an instrumented research aircraft are presented. Aerosol number densities and volume are computed over a range of particle diameters from 0.1 to 200 μm, while the sea surface conditions, including H_s, moments of the breaker length distribution $\Lambda(c)$, and wave breaking dissipation, were measured by a suite of electro-optical sensors that included the NASA Airborne Topographic Mapper (ATM). The sea-state dependence of the aerosol concentration in the MABL is evident, stressing the need to incorporate wave parameters in the spray source generation functions that are traditionally parameterized by surface winds alone.

1. Introduction

Sea spray aerosols represent a significant fraction of the aerosol particles that exist in the maritime atmosphere. Despite extensive work and remarkable progress in the last two decades, mostly motivated by cloud microphysics, atmospheric chemistry, regional and global climate modeling, and the direct and indirect radiative effects of marine aerosols, our understanding of the mechanisms through which spray is ejected from the surface and transported in the marine atmospheric boundary layer (MABL) and then higher up in the atmosphere remains very limited. Scatter in sea spray source functions span more than an order of magnitude (de Leeuw et al. 2011; Veron 2015), especially for the larger particle sizes. Transport and generation mechanisms for the latter are poorly understood. In their review of sea spray source function parameterized from laboratory and field experiments on sea spray aerosol production, de Leeuw et al. (2011) showed that there remain large uncertainties in the sea spray source generation functions (SSSGFs). Most SSSGFs of marine aerosols are traditionally parameterized by wind speed (Smith et al. 1993; Fairall et al. 1994; Lewis and Schwartz 2004). Hanley et al. (2010) conducted a global climatology of wind-wave interaction based on a 40-yr ECMWF Re-Analysis (ERA-40) dataset. They found that there were few occurrences of wind-wave equilibrium, even in the Southern Ocean and northern latitude trade wind regimes. This was due in part to the presence of swell but also due to the variability of the winds. In short, one cannot assume that wave effects that might be included at equilibrium are included in general.

Few studies have investigated the use of wave breaking characteristics as a proxy: whitecap coverage (Monahan et al. 1986; Mårtensson et al. 2003; Norris et al. 2013a) and distribution of lengths of surface breaking fronts (Mueller and Veron 2009) based on Phillips (1985) formulation.

Recent work has explored the use of a range of wave-state parameters in formulating SSSGFs. Norris et al.

Denotes Open Access content.

Corresponding author e-mail: Luc Lenain, llenain@ucsd.edu

DOI: 10.1175/JPO-D-16-0058.1

(2013b) and Ovadnevaite et al. (2014) use a wave Reynolds number, originally introduced by Zhao and Toba (2001; see also Zhao et al. 2006). In most of these studies, wave measurements are limited, making the inclusion of wave parameters into the SSSGF formulation very challenging.

Though important for the global aerosol budget and biochemical aspects of ocean–atmosphere interaction processes, the mechanisms through which larger sea spray aerosols, of diameters greater than 20 μm, are generated and transported into the MABL remain poorly understood, leading to significant uncertainty regarding the contribution of spray-mediated fluxes to the total air–sea fluxes for such size ranges. Laboratory experiments (e.g., Fairall et al. 2009; Veron et al. 2012) have focused on the generation and dispersion mechanisms of such droplets, but field measurements in this size range are very sparse, especially at height, within the MABL. Recent LES modeling (Shpund et al. 2011, 2012, 2014) showed that large eddies play a crucial role in transporting large spray aerosols vertically to heights of several hundred meters above the ocean surface, significantly impacting the vertical dynamics and cloud microphysical structures in tropical cyclones (Shpund et al. 2014).

Evidence of large concentrations of marine aerosols well above the ocean surface has been documented in severe weather environments. Following a nearly catastrophic failure of a NOAA WP3D aircraft that lost power to three of its four engines in the North Atlantic Ocean flying at approximatively 800 m above mean sea level (MSL) in a hurricane force wind region, Reid et al. (2007, p. 1) concluded in their postincident assessment that

> sea salt aerosol particles generated in the high winds and high (up to 20 m) seas coated the aircraft and caused severe engine fouling resulting in compressor stalls.

In the present study, detailed, coincident, and collocated field measurements of aerosols of diameters ranging from 0.1 to 200 μm, waves, wave kinematics, and atmospheric conditions were gathered over a range of wind speeds and wave conditions, providing a rare opportunity to investigate the relationship between aerosol concentration in the MABL and both atmospheric and sea-state conditions.

We find guidance from the scaling of breaking by Sutherland and Melville (2013) that has its roots in the inertial scaling of breaking by Drazen et al. (2008) and Romero et al. (2012). This influences the dimensional analysis that leads to the best collapse of the data from both the High-Resolution Air–Sea Interaction Experiment (HIRES) and Gulf of Tehuantepec Experiment (GOTEX) with a dependence on both wind and wave parameters.

In section 2, the HIRES experiment and the instrumentation are presented. In section 3, following a brief presentation and analysis of the measurement, we present a dimensionally consistent equation for the aerosol concentration. The results are summarized in section 4.

2. Experiment and methods

The results presented here were collected from a *Twin Otter* research aircraft, from the Center for Remotely Piloted Aircraft Studies (CIRPAS), in June 2010 during the main field campaign of the Office of Naval Research HIRES Departmental Research Initiative (DRI), off the coast of northern California (Grare et al. 2013).

In addition to carrying a basic navigation and meteorological system, the aircraft was outfitted with a suite of aerosol particle size sensors, atmospheric turbulence sensors, and surface wave and surface kinematics instrumentation. The aircraft flight team is specifically trained to conduct low level flights over the ocean, down to 30 m MSL in high-wind conditions for extended periods of time. Figure 1 shows the environmental conditions experienced during the experiment, measured from the closest meteorological buoy (NDBC 46013) and Research Platform (R/P) *Floating Instrument Platform* (*FLIP*), which was moored 25 km off the California coast (38°20′N, 123°26′W) for part of the experiment (see Fig. 2g). The flight times are highlighted in yellow, covering a broad range of environmental conditions with U_{10} ranging from 8 to 18 m s^{-1} and H_s from 2 to 4.5 m. The low-level tracks for two of the considered flights (out of a total of 8 flight-days), on 15 and 30 June 2010, are shown in Fig. 2g. Note that low-level track data were analyzed for all 8 flight-days, corresponding to a total of approximately 3 flight-hours out of the total 32 flight-hours we flew at the experiment site during the project.

a. Aerosol instrumentation

Aerosol measurements were made using a suite of sensors installed on wing pylons to provide in situ sampling of the particles present in the airflow. The instrument pod is shown in Fig. 2b. A Passive Cavity Aerosol Spectrometer Probe [PCASP-100X, Particle Measuring Systems, Inc. (PMS)] and a forward Scattering Scatterometer Spectrometer Probe (FSSP-100, PMS) measured particle size (diameter) from 0.11 to 2.124 μm and 2.37 to 28.24 μm, respectively, over 20 size bins for each system. A cloud aerosol precipitation spectrometer [CAPS, Droplet Measurement Technologies (DMT)] and a cloud imaging probe (CIP, DMT), sampled the larger aerosol particles of diameters ranging from 0.62 to 53.72 μm and 25 to 1550 μm over 20 and 62 size bins, respectively. All instruments were

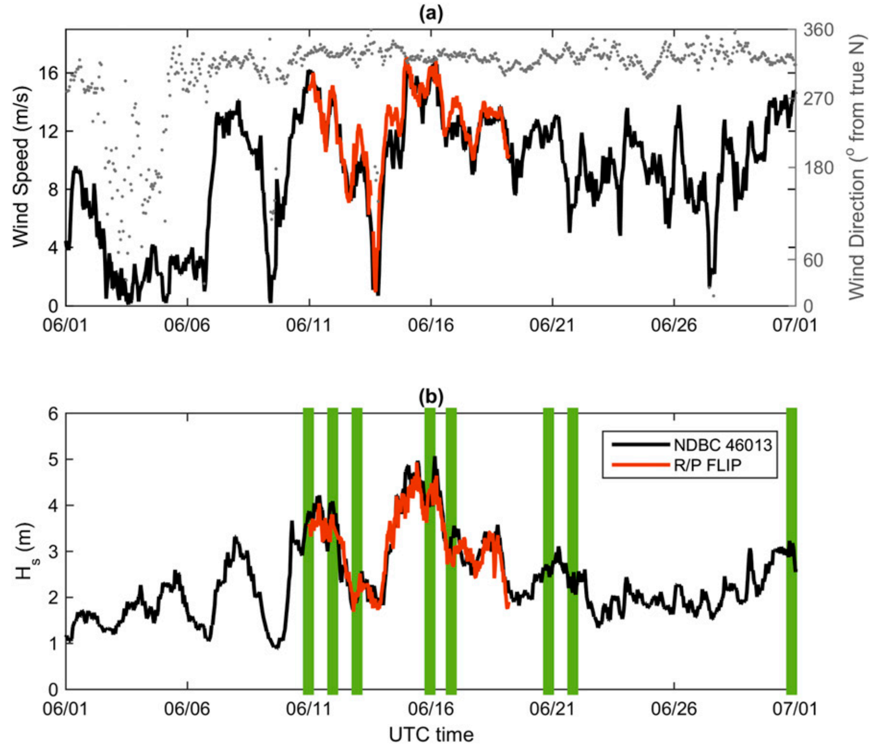

FIG. 1. (a) Wind speed and direction and (b) significant wave height H_s (m) for the month of June 2010 at NDBC 46013, the closest meteorological buoy to the HIRES experiment site, and the corresponding measurements from R/P *FLIP* (red). The time of the CIRPAS aircraft research flights considered in this study are highlighted in green.

calibrated prior to and after the field deployment at the CIRPAS calibration facility, accurately characterizing the lower and upper bounds of each size-range channel for all four sensors.

b. *Wave and surface kinematics*

The sea surface elevation was measured with a scanning lidar instrument: the National Aeronautics and Space Administration (NASA)/EG&G Airborne Topographic Mapper (ATM III). Although this system is primarily used to characterize ice sheet thickness in polar regions as part of the NASA Ice Bridge project (Krabill et al. 1995), the ATM has proven to be an excellent tool to measure directional wave fields in past experiments (Hwang et al. 2000a,b; Romero and Melville 2010a,b; Romero et al. 2012). During HIRES, the ATM's conical scanning angle was set to 22° with a pulse repetition rate of 5 kHz and a scanning frequency of 20 Hz. In addition, a suite of nadir-looking, high-resolution visible and infrared imagers provided information about surface kinematics and wave breaking.

Though the ATM lidar was not designed for atmospheric measurements, careful analysis of the waveform signal collected for each laser pulse sent and received by the sensor was conducted to identify partial or spurious returns from aerosols above the ocean surface. A similar approach was tested in a laboratory setting in recent work from Toffoli et al. (2011). Note that the ATM laser wavelength is 532 nm (green) and therefore can penetrate the first few meters of the water column. Similar lasers have been used for biochemical remote sensing both from aircraft and ships (e.g., Churnside et al. 1998, 2001; Brown et al. 2002; Carrera et al. 2006). Figure 3 shows a large breaking event captured from the ATM lidar and nadir-looking video camera, installed on the aircraft, in the vicinity of R/P *FLIP* during the HIRES experiment on 15 June 2010 at 2301 UTC. The wind speed U_{10} measured from *FLIP* was 14.8 m s^{-1} at that time. The transverse length scale for this particular breaker is large, reaching close to 85 m, for a crest to trough individual wave amplitude of 7.2 m, implying the generation of a significant amount of aerosols during the breaking process. The data collected from the airborne system are split in two, corresponding to Figs. 3a and 3b, to differentiate between the data collected forward and aft of the aircraft location (recall that the ATM has a circular scan pattern). This results in the lidar (as well as the camera) effectively scanning the same area at two

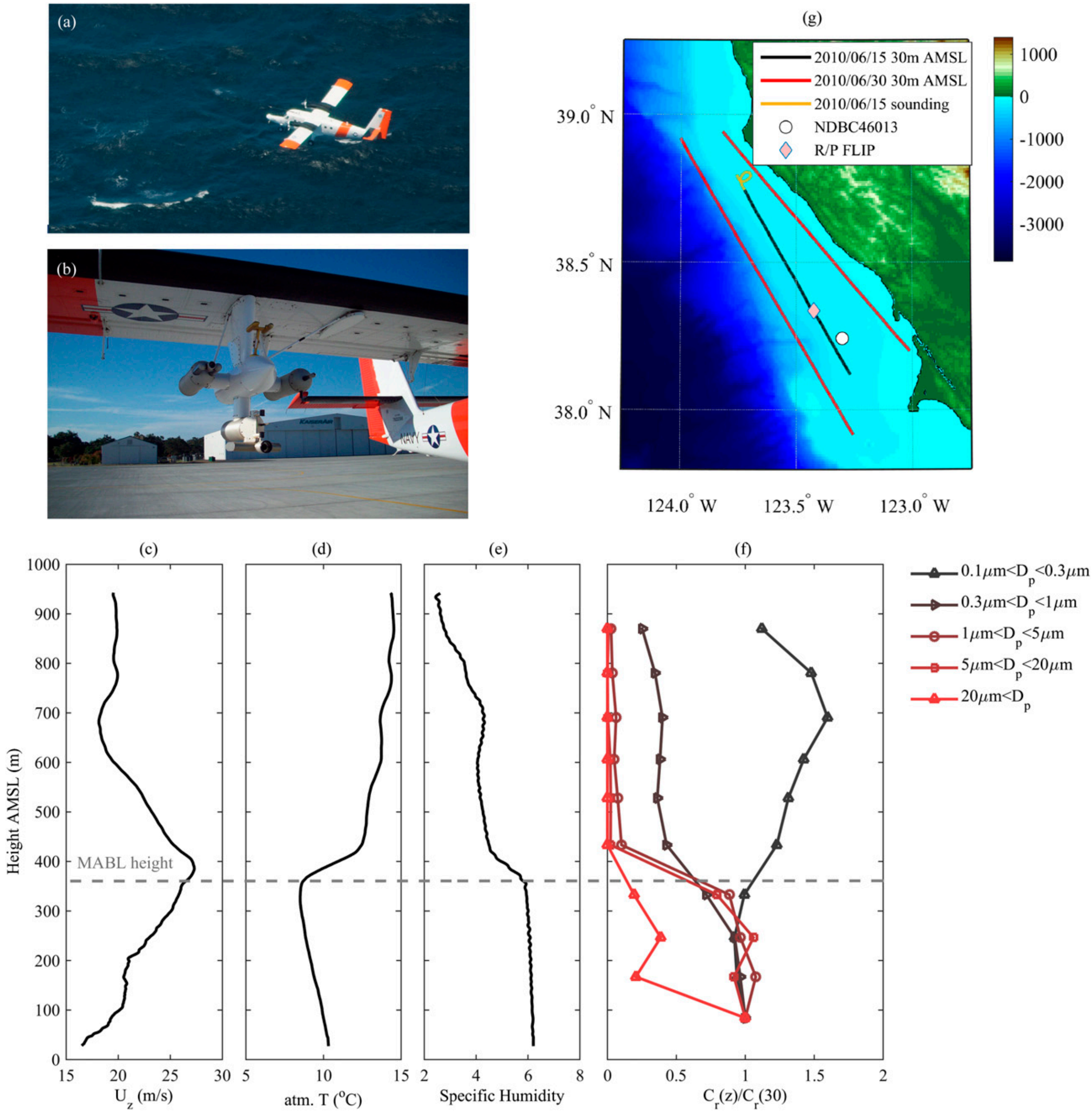

FIG. 2. (a) CIRPAS *Twin Otter* flying at 30 m MSL during the ONR HIRES2010 experiment. (b) Aerosol sampling instrumentation mounted on the starboard wing of the aircraft (PCASP + CIP + CAPS + FSSP). (c)–(f) Vertical profiles of wind speed ($m\,s^{-1}$), atmospheric temperature (°C), specific humidity, and aerosol concentration for five diameter ranges, respectively, collected on 15 Jun 2010 during one of the sounding portions of the flight, depicted as an orange color track in (g). (g) Bathymetric map of the operation area showing three of the 30 m MSL flight tracks considered in the present analysis, and the location of R/P *FLIP* and the NDBC 46013 meteorological buoy during the experiment.

different times, separated by a δt, which depends on flight altitude, aircraft speed, and the azimuthal position of the lidar beam. Here, δt was approximately equal to 5 s for the transect shown in the figure. The two lower panels show a cross section corresponding to the transect shown in the plan view plotted in the upper panels. Surface elevation is shown in red while returns from aerosols are shown as black dots. The active part of the breaking wave corresponds to the area where the number of aerosol returns increases. This result, though very qualitative, reinforces the need to incorporate some characteristics of the wave field in aerosol production

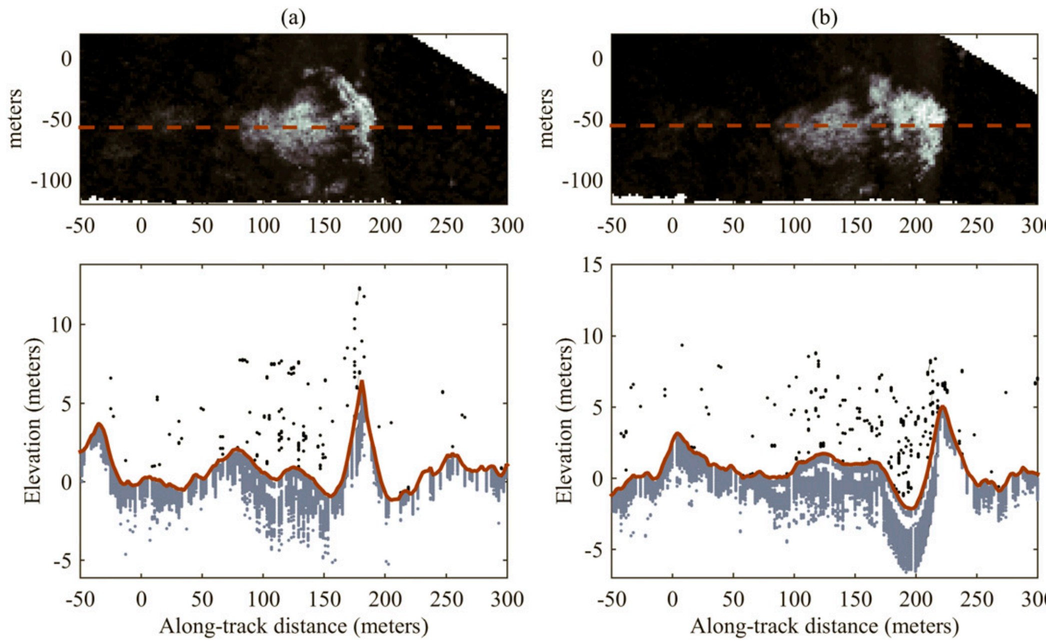

FIG. 3. Large breaking wave event captured with the ATM lidar and collocated video camera on 15 Jul 2010 at 2301 UTC during the HIRES experiment. The same wave at instant (a) $t = t_o$ and (b) $t = t_o + \delta t$, where $\delta t = 5$ sec. The two bottom panels show the surface elevation (red) corresponding to the transect shown as a dashed line in the two upper panels. ATM waveform outlier returns, a proxy for the presence of larger aerosols or bubbles, are also plotted as blue (bubbles below the water surface) and black (above the water surface) dots. Note the persistent returns below the surface likely from the underlying bubble layer and plume from the breaker.

models, especially the effects due to wave breaking. Also note the presence of lidar returns below the surface (blue dots), likely associated with the presence of a bubble plume right below the breaking wave.

In addition, a nadir-looking fixed lidar altimeter (Riegl LD90–3800VHS) provided measurements of sea surface displacement when flying at altitudes between 30 and 200 m above mean sea level, below the minimum range of the ATM. The altimeter was set to sample at 1 kHz, averaged down to 100 Hz to improve the signal-to-noise ratio.

3. Measurements

The flight profiles for each sortie included periods of time flying at the lowest permitted altitude, typically 30 m MSL, with its reciprocal track at 300 m MSL altitude to permit directional wave measurements and surface kinematics from the nadir-looking, electro-optical system and helical soundings at the beginning and end of each flight leg from 30 to 1000 m to characterize the structure of the MABL. A representative example of (Fig. 2c) wind speed at z meters MSL U_z (m s^{-1}), (Fig. 2d) atmospheric temperature T (°C), and (Fig. 2e) specific humidity q (dimensionless) as a function of height z (m) MSL collected on 15 June 2010 at the northern end of an upwind flight leg is shown in Fig. 2. Figure 2f shows the measured fraction of aerosol concentration relative to the measurements at 30 m MSL for five ranges of diameter d, from 0.1 to 20 μm and larger sizes. The MABL extends at that time to approximately 400 m MSL (see Figs. 2c–e). Aerosols of diameter ranging from approximately 1 to 20 μm show an approximately constant concentration within the MABL and rapidly drop to zero above it. The smaller particles, with diameters $d < 1\,\mu$m, while also close to constant concentration as a function of height inside the MABL, show an increased concentration above the MABL likely associated with other sources not related to the air–sea interface. Larger aerosols (>20 μm) are present in the MABL, but their concentration rapidly decreases with increasing height.

a. Aerosol distributions

We define the size distribution function $n(d)$ such that $n(d)dd$ is the number of aerosol particles per unit volume of air having diameters in the range d to $d + dd$, where dd indicates the differential with respect to d. The total number of particles per unit volume of air is therefore

$$N = \int_0^\infty n(d)\, dd\,. \tag{1}$$

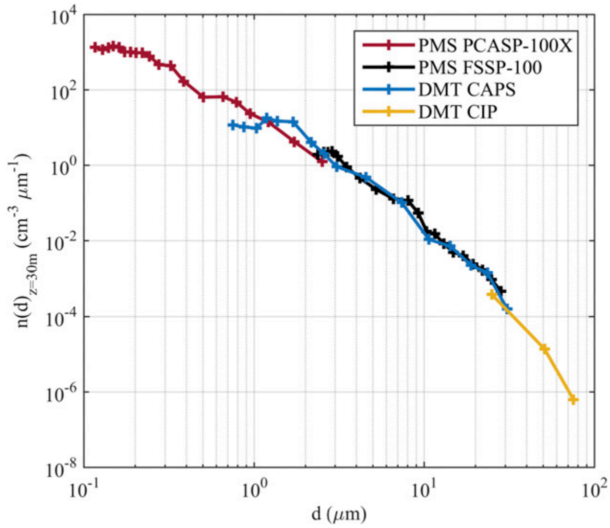

FIG. 4. Representative example of aerosol number distributions taken on 15 Jul 2015 2010 at 2330 UTC during the HIRES experiment, showing the overlap between the four sensors: PMS PCASP-100X (red), DMT CAPS (blue), PMS FSSP-100 (black), and DMT CIP (yellow).

Our measurements are obviously discrete and limited to a set range of aerosol diameters; the measured number of particles in the size range d to $d + dd$ is defined as $dN = n(d)dd$, leading to the more commonly used expression of the aerosol number distribution dN/dd. Surface area, volume, and mass distribution of aerosols are of particular interest, as a number of aerosol properties depend on these variables. While the aerosol surface is where thermal, gas, and chemical exchanges occur, the aerosol volume density characterizes the amount of seawater and its content transferred to the atmosphere by marine aerosols. In the present study, we focus on the relationship between sea-state conditions and size and volume distributions of marine aerosols.

Figure 4 shows an example of aerosol number distribution computed from the four aerosol instruments considered during a 6-km segment flying at 30-m altitude. Overall, we find good agreement between all sensors.

We define the aerosol volume distribution $n_v(d)$ as the volume of particles per unit volume of air having diameter in the range d to $d + dd$, where

$$n_v(d) = \frac{\pi}{6} d^3 n(d), \tag{2}$$

such that the total volume of aerosol per volume of air[1], that is, the total aerosol volumetric concentration V is

[1] For consistency with the literature, we consider here the volume of air and not the volume of the air and aerosol, as the difference is negligible.

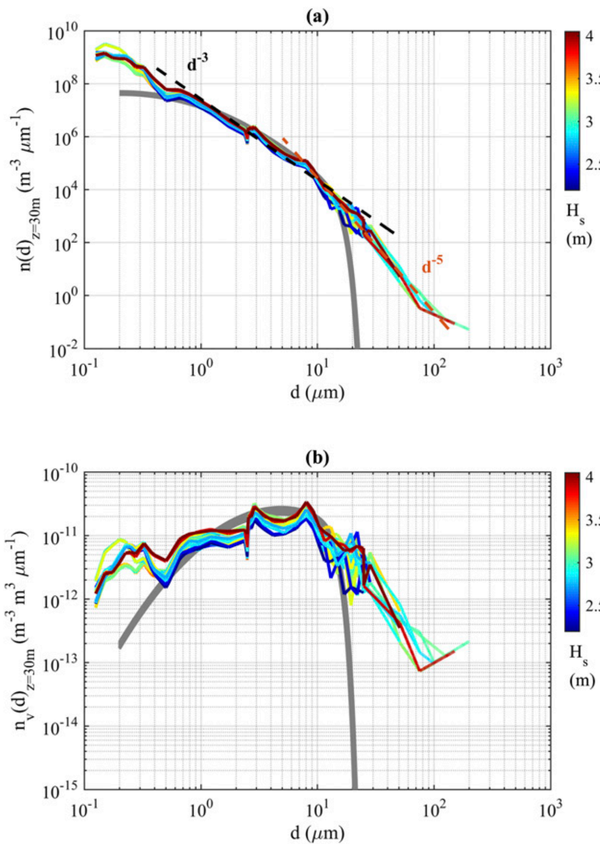

FIG. 5. (a) Aerosol number distributions collected from the instrumentation mounted on the CIRPAS *Twin Otter* during the low-level flights (30 m MSL) for a wind speed $U_{10} = 15 \pm 1\,\mathrm{m\,s^{-1}}$. Distributions are color-coded for H_s. Shown in gray is the predicted aerosol number distribution at the same altitude based on an empirical SSSGF described in Lewis and Schwartz (2004), assuming that the vertical transport of droplets by turbulence is balanced by gravitational settling for the same surface wind speed (Fairall et al. 2009; Veron 2015). (b) Corresponding aerosol volume distributions.

$$V = \frac{\pi}{6} \int_0^\infty d^3 n(d)\, dd. \tag{3}$$

Figure 5a shows the aerosol size distributions collected from the *Twin Otter* instrumentation for a selected wind speed $U_{10} = 15 \pm 1\,\mathrm{m\,s^{-1}}$ during all considered flights and color-coded for H_s. The significant wave height H_s is computed from the surface displacement η measured by the nadir-looking laser altimeter, such that $H_s = 4\eta_{\mathrm{rms}}$, where η_{rms} is the root-mean-square surface elevation. Note the two power laws: d^{-3} for $1 < d < 10\,\mu$m and rolling off to a d^{-5} power law for the aerosols of larger diameter. These measurements are compared against an empirical source concentration function to verify that the observed concentration levels are generally consistent with accepted aerosol marine source functions. Note that this approach is far from ideal, as it requires crude assumptions and simplifications of the transport mechanisms through which the aerosols are transported into the MABL. The lack of consensus and basic understanding of the physics involved in the transport mechanisms, in particular for the larger particles, is in fact the primary motivation for not computing aerosol production fluxes in the present study, by extrapolating our measurements at height to the surface. The following comparison should therefore not be taken as a detailed validation but rather a consistency check. Here, we use an empirical source concentration function at the surface defined by Lewis and Schwartz (2004) in a similar approach to the one used in Jones and Andreas (2012) as

$$n_o = \frac{dN}{dr_{80}} = \frac{7\times10^4 U_{10}^2}{r_{80}} \exp\left\{-\frac{1}{2}\left[\frac{\ln(r_{80}/0.3)}{\ln(2.8)}\right]^2\right\} \tag{4}$$

for the same range of wind speed U_{10}. Here, r_{80} is the equilibrium aerosol radius at an equivalent 80% relative humidity. This radius is commonly used to characterize smaller diameter aerosols to account for the exchange of moisture between the hygroscopic drop and its surrounding. It is assumed here that the aerosols reach equilibrium by the time they are sampled, such that $d = 2r_{80}$. As the measurements presented here were collected well above the source region ($z = 30$ m), we need to assume a transport mechanism from the source to the measurements' height. Fairall et al. (2009) suggest that the vertical transport of droplets by turbulence is balanced by the gravitational settling velocity v_d leading to

$$n(d,z) = n_o(d)\left(\frac{z}{h_o}\right)^{(-v_d \mathrm{Sc}_t)/(\kappa u_* f_s)}, \tag{5}$$

where h_o is the upper limit of the source region, Sc_t is the droplet's turbulent Schmidt number, and f_s is a slip coefficient first introduced by Rouault et al. (1991). Here, u_* is the atmospheric friction velocity, computed iteratively from the wind speed measured at the 30-m flight altitude U_{30} using TOGA COARE 3.0 (Fairall et al. 2003), assuming a constant flux layer with a logarithmic wind profile:

$$U_z = \frac{u_*}{\kappa}\ln\left(\frac{z}{z_o}\right), \tag{6}$$

where z is the measurement height above mean sea level, and z_o is the roughness length. Here, we use the most recent parameterization implemented in TOGA COARE 3.0, which utilizes a characteristic of the wave field, the wavelength at the peak of the wave spectrum λ_p, based on Oost et al. (2002), as described in Fairall et al. (2003):

$$z_o = \frac{50}{2\pi}\lambda_p\left(\frac{u_*}{c_p}\right)^{4.5} + \frac{0.11\nu_a}{u_*}, \tag{7}$$

where ν_a is the kinematic viscosity of air. Equation (6) is also used to compute the wind speed at 10 m U_{10} from the measurements at the 30-m flight altitude.

The velocity v_d is defined as

$$v_d = \frac{\rho_w d^2 g}{18\mu} C_c, \tag{8}$$

where ρ_w is the density of seawater, g is the gravitational acceleration, and μ is the viscosity of air; C_c is the so-called Cunningham factor (Cunningham 1910), a correction factor needed to account for the reduced slippage at the particle surface for aerosol diameters smaller than 1 μm. It is defined as

$$C_c = 1 + \frac{2.52\lambda}{d}, \tag{9}$$

where λ is the mean free path of molecules of gas (in our case air).

The aerosol concentration at $z = 30$ m derived from the empirical formulation described in Eqs. (4) and (5) are shown in gray in Fig. 5. Here, h_o was set to the significant wave height H_s, and Sc_t is taken to be equivalent to that for water vapor (Rouault et al. 1991). While our measurements agree with the general shape of the distribution derived from the empirical formulation described above for $0.5 < d < 15\,\mu$m, significant differences are shown above and below that range. For the smaller range of aerosol diameters, $d < 0.5\,\mu$m, the measured concentration is higher, likely due to the presence of a nonlocal source of aerosols (marine or even perhaps terrestrial). The largest differences are found for droplet diameters $d > 15\,\mu$m. The simplified vertical transport model considered here, taken here as u_*, is not large enough to balance the droplet settling velocity for those larger droplets. The simple fact that large diameter aerosols are found well above the marine aerosol source layer implies that other transport mechanisms (e.g., initial ejection velocity from the jet drops, large eddies) need to be considered to explain how those droplets are found at such altitudes.

b. Ocean surface kinematics and breaking statistics

Wave breaking plays a fundamental role in the generation of marine aerosols. Spume drops are ejected from breaking waves when the wind speed is high enough, the toe of plunging breakers generate spray on impact with the surface below, while bursting bubbles from the subsurface bubble plume generated during the wave breaking process produces film and jet drops (Veron 2015; Andreas 1995). Phillips (1985) introduced the length of breaking fronts $\Lambda(c)$ and its moments to characterize breaking statistics. The first moment R,

$$R = \int c\Lambda(c)\, dc, \tag{10}$$

represents the fraction of ocean surface turned over by breaking fronts per unit time. Phillips (1985) [see also Duncan (1981)] also defined the total energy dissipated by breaking waves (per unit area of ocean surface) as

$$F = \frac{\rho_w}{g}\int b(c)c^5\Lambda(c)\, dc, \tag{11}$$

where b is the nondimensional breaking parameter. Based on the inertial scaling and laboratory data of Drazen et al. (2008) and Melville (1994) and laboratory data of Banner and Pierson (2007), Romero et al. (2012) computed a dimensionless breaking parameter that uses the azimuth-integrated surface wave saturation spectrum $B(k)$ defined as

$$B(k) = \int_{-\pi}^{\pi} \phi k\, d\theta\, k^3, \tag{12}$$

where $\phi(k, \theta)$ is the directional surface wave spectrum: with θ the azimuthal direction (coming from) and k the surface wavenumber.

The term $b(k)$ is then defined as

$$b(k) = A_1[B(k)^{1/2} - B_T^{1/2}]^{1/2}, \tag{13}$$

where B_T is a threshold saturation, and A_1 is a constant defined in Romero et al. (2012). This approach is supported by recent theoretical work from Pizzo and Melville (2013). Then $b(c)$ was computed from $b(k)$, assuming a linear dispersion relationship for gravity waves: $c = (g/k)^{1/2}$. Also, note that in this analysis we approximate the speed of the breaker c as the phase speed of the underlying wave.[2]

Directional wavenumber spectra $\phi(k, \theta)$ are computed from the sea surface displacement data collected with the ATM. Here, 6-km swath lengths are used for the analysis, typically 250 to 300 m wide in the cross-track direction, using only the forward portion of the ellipsoidal scanning pattern.[3] Each data subset is regridded to a 2.5-m horizontal spatial resolution using 2D linear interpolation, leading to an approximately 1.26 rad m^{-1} cutoff wavenumber. We found that the noise level typically started at lower wavenumbers, around 0.8–1 rad m^{-1}; the measured spectrum above this value was therefore discarded. The measured directional wavenumber spectra are extrapolated toward larger wavenumbers, up to 30 rad m^{-1}, using a k^{-4} power law that matches a constant saturation regime for the larger wavenumbers. This extrapolation is needed as a significant portion of the wave breaking dissipation lies in the 1 to 30 rad m^{-1} range (Romero et al. 2012; Sutherland and Melville 2013). A sample omnidirectional and saturation spectrum is shown in Fig. 6.

The $\Lambda(c)$ distributions are computed from the nondimensional scaling derived by Sutherland and Melville (2013), where the nondimensional Λ distribution $\hat{\Lambda}(\hat{c})$ is given by

$$\hat{\Lambda}(\hat{c}) = \Lambda(c)c_p^3 g^{-1}\left(\frac{c_p}{u_*}\right)^{0.5} = 0.05 \times \hat{c}^{-6}, \tag{14}$$

and

$$\hat{c} = \left(\frac{c}{\sqrt{gH_s}}\right)\left(\frac{gH_s}{c_p^2}\right)^{0.1}. \tag{15}$$

Here, c_p is the phase speed of the waves at the peak frequency and H_s is the significant wave height, both computed from the ATM measurements; $\sqrt{gH_s}$ is the speed at impact of a particle following a ballistic trajectory from a height $H_s/2$; c_p/u_* is the wave age; and gH_s/c_p^2 is a characteristic wave steepness, also called the significant wave slope.

Measurements of the $\Lambda(c)$ distribution computed from the nadir-looking video imager installed on the aircraft for a selected number of representative portions of the flights were consistent with the scaling defined above by Sutherland and Melville (2013). A representative example is shown in Fig. 7. Based on the agreement of this scaling with the measurements, we use the formulation from Sutherland and Melville (2013) to compute the breaking distribution in the subsequent analysis. Note that the range of c was taken to be from 0.1 to 30 m s^{-1} for the wave breaking dissipation computation and from 3 to 30 m s^{-1} for the first

[2] Field measurements of the speed of breaking fronts are typically found in the [0.8–1]c range.

[3] No significant differences were found between the spectra computed from the rear and forward scans computed over the same area.

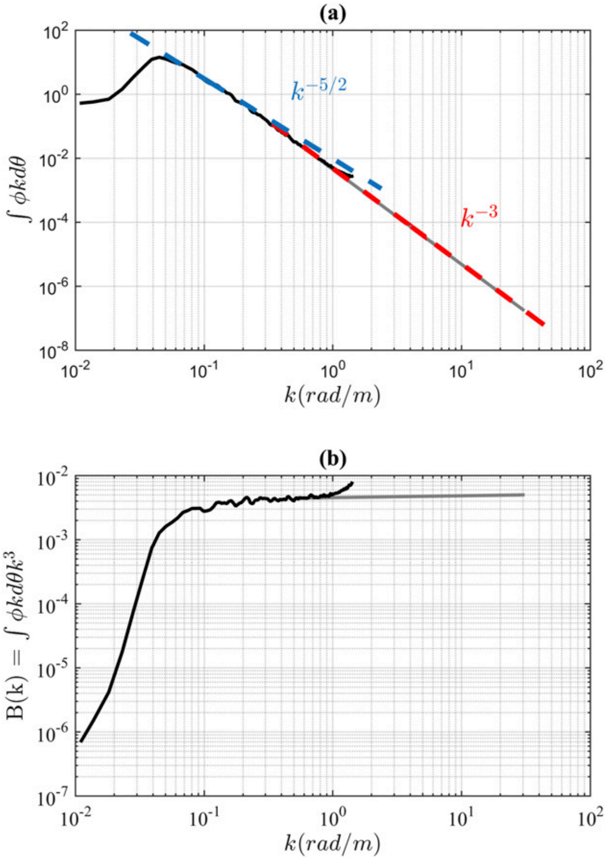

FIG. 6. (a) Sample omnidirectional wavenumber spectrum collected on 15 Jun 2010 during the HIRES experiment. The measured spectrum with a high-wavenumber cutoff at 1.2 rad m^{-}, is shown in black, while the spectrum, extrapolated to 30 rad m^{-1}, used in the computation of the energy dissipated by breaking waves [see Eq. (11)] is shown in gray. Note the −5/2 and −3 spectral slopes. (b) Corresponding saturation spectra $B(k)$.

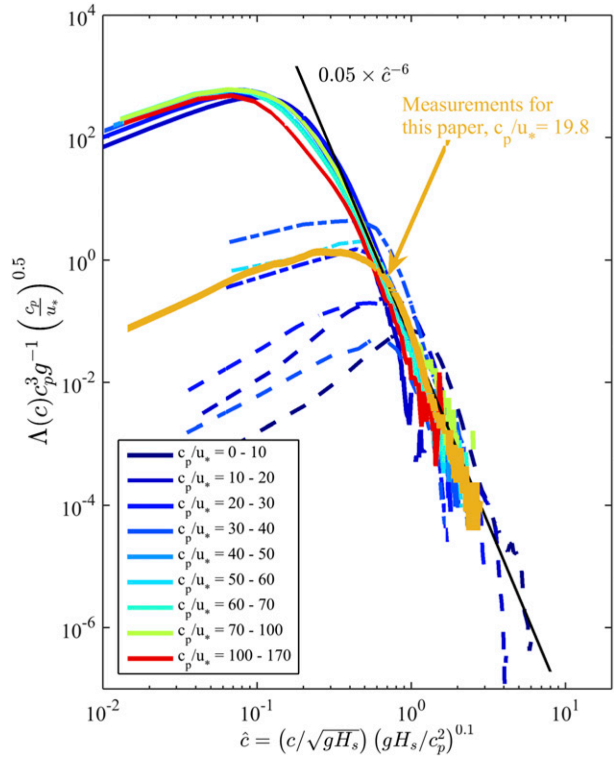

FIG. 7. Representative example of nondimensional breaking length distribution computed from the airborne imagery collected on 11 Jul 2015 2010 at 0120 UTC during the HIRES experiment (orange solid line), overlaid on the nondimensional breaking distributions presented in Fig. 4 of Sutherland and Melville (2013). Distributions have been binned by wave age with corresponding colors. Solid lines are measurements taken using stereo IR imagery, dashed–dotted lines are from visible imagery, both collected from R/P *FLIP*, and dashed lines are from the airborne measurements of Kleiss and Melville (2010) during GOTEX.

moment of the $\Lambda(c)$ distribution, with phase speeds large enough to produce air entrainment during the breaking process (Sutherland and Melville 2013).

c. Dependence of aerosol concentration on local atmospheric and sea-state conditions

The aerosol concentration measured at 30 m above the mean sea level is expected to be influenced by nonlocal sources but mostly for the smaller diameter particles that can travel over long distances for extended periods of time. Because of the measurement altitude considered here (30 m MSL), we can safely assume that most particle concentration measured at this height, under the considered range of conditions (2- to 4.5-m significant wave height and 8 to 18 m s^{-1} wind speed), will be correlated with the local conditions. A simple estimate can be made based on the mean vertical Lagrangian velocity in a logarithmic boundary layer, which is $O(u_*)$, the friction velocity in the air. Now, $u_* = \sqrt{C_D}U_{10}$, where the usual notation holds. Thus, the average time for a small particle to reach a height H is just H/u_*, and the horizontal distance traveled is just

$$X = \int_0^{H/u_*} U(z = u_* t)\,dt. \tag{16}$$

If U_{10} is used to scale the horizontal velocity over heights of $O(10)$ m, then $X \approx O(H/\sqrt{C_D})$. So for H = 30 m and $C_D = O(10^{-3})$, we have that the horizontal distance traveled from the surface to 30 m is of the order of 1 km. This is the scale of the length of wave groups, the scale over which large breaking events are observed (Terrill and Melville 1997; see also Fig. 3 of the current paper). Furthermore, given the potential significance of the large initial velocities associated with breaking events, it is likely that this is an overestimate for some

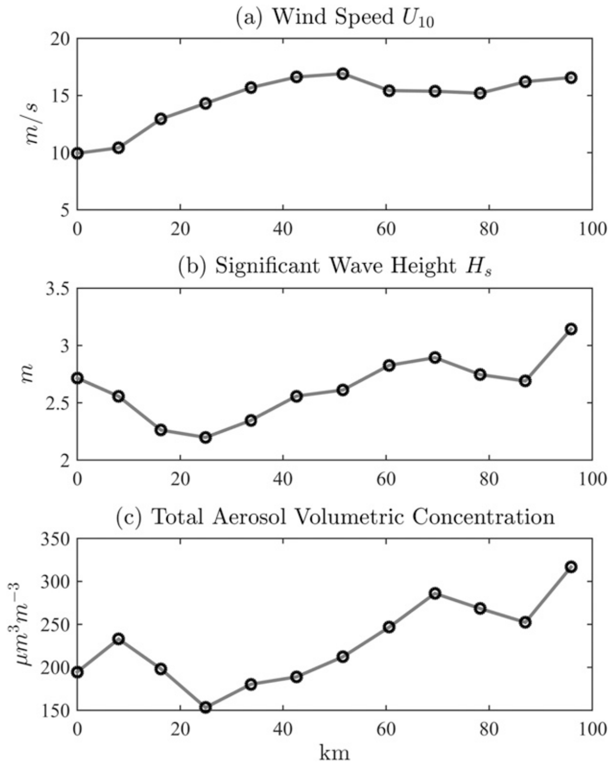

FIG. 8. (a) Wind speed U_{10} (m s^{-1}), (b) significant wave height H_s (m), and (c) total aerosol volumetric concentration V(μm^3 m^{-3}) measured during a 95 km, straight, 30 m MSL flight section on 30 Jun 2010.

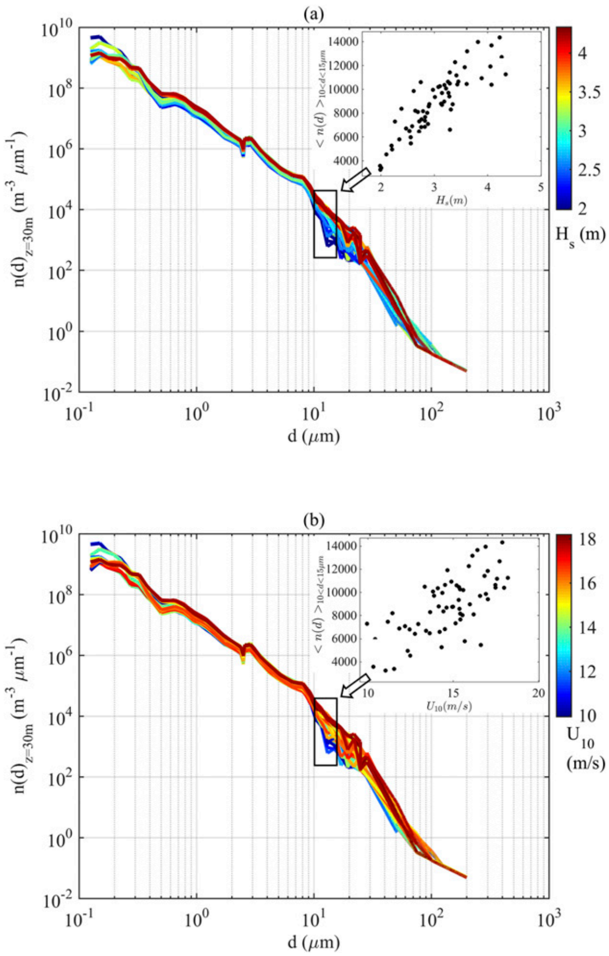

FIG. 9. Aerosol size distributions for all HIRES2010 low-level flights (30 m MSL) color-coded for (a) significant wave height H_s (m) and (b) 10-m wind speed U_{10} (m s^{-1}). The inserts show the distribution level for an aerosol range diameter of 10 to 15 μm as a function of H_s in (a) and U_{10} in (b), illustrating the increased scatter in the aerosol size distribution levels when plotted as a function of wind speed.

range of particle sizes. Figure 8 illustrates the influence of local conditions on the aerosol volumetric concentration, where time series of wind speed U_{10}, significant wave height H_s, and total aerosol volumetric concentration V (aerosol diameters ranging from 0.1 to 200 μm) measured during a 95-km straight portion of flight (approximately 24-min flight time) at 30 m MSL on 30 June 2010 is shown. Each value is computed over a 6-km record of collected data. We find here that not only the total aerosol volumetric concentration generally better correlates with significant wave height and not wind speed, but the rapid response to the local changes in sea-state conditions by the aerosol concentration data is remarkable, again stressing the need to incorporate local sea-state information in SSSGF parameterization.

Figure 9 shows the aerosol number density distributions $n(d)$ collected during all low-level flights (30 m MSL) over the range of environmental conditions experienced during the HIRES 2010 experiment. Each distribution is computed over a 6-km record of data collected from all available aerosol sensors described earlier, then interpolated over a regularly spaced range of diameters d ranging from 0.1 to 200 μm with 0.025-μm increments.

The aerosol number density distribution plotted in Fig. 9a is color-coded for the significant wave height H_s computed from the nadir-looking lidar altimeter data over the same record length. Starting from diameters d larger than 0.3 μm, the aerosol distributions show a nicely organized dependence on the significant wave height, with levels increasing as H_s increased from 2 to almost 4.5 m. In Fig. 9b, the same distribution is shown, but this time color-coded for U_{10}. In that case, the relationship between distribution levels and wind speed is much less organized. The two inserts show the distribution levels for an aerosol size range of 10 to 15 μm to illustrate the increased scatter with U_{10}.

The total aerosol volumetric concentration V measured over the 0.1- to 200-μm diameter range considered

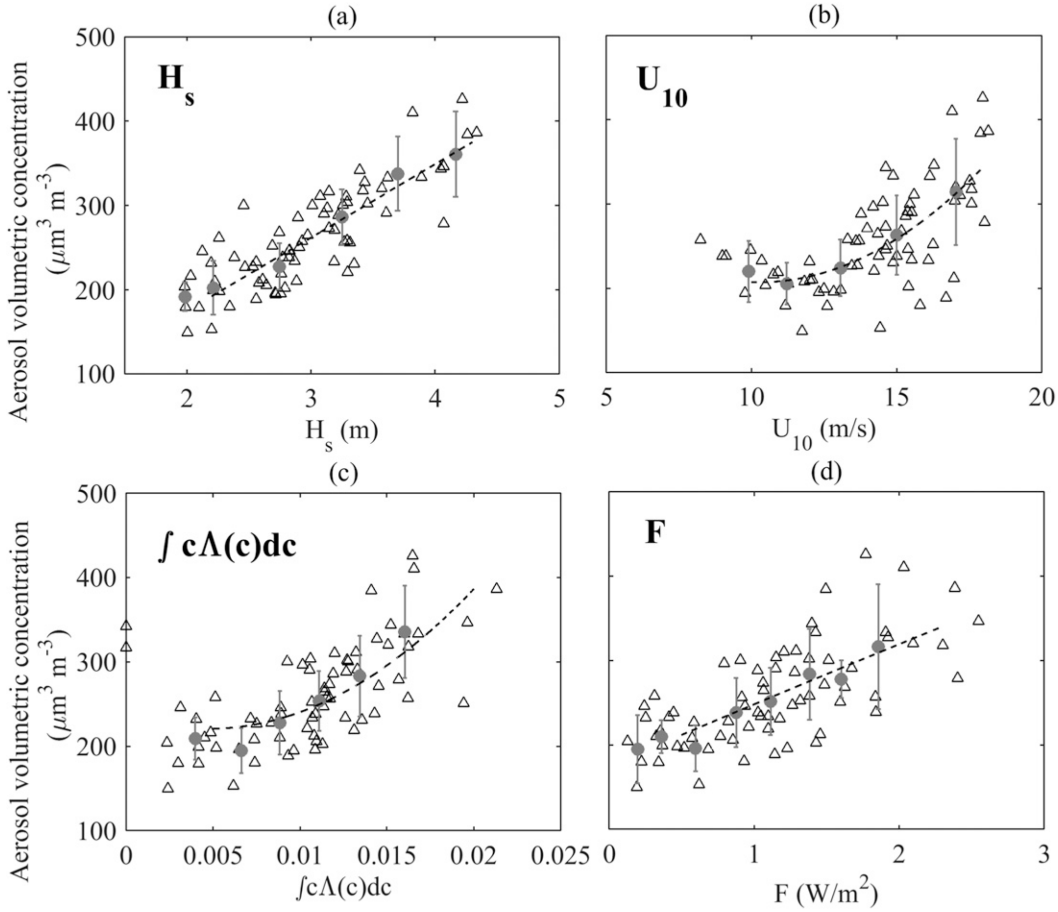

FIG. 10. Total volume of aerosols measured during the HIRES 30 m MSL flight sections as a function of (a) significant wave height H_s (m), (b) wind speed U_{10} (m s^{-1}), (c) first moment of the $\Lambda(c)$ distribution, and (d) computed dissipation by wave breaking F (W m^{-2}). The gray dots represent the corresponding bin-averaged values (with associated error bars), while the dashed line represents the fit of the data [(a) and (d) are linear; (b) and (c) are quadratic].

here during the low altitude (30 m MSL) portions of the flights is shown in Fig. 10 as a function of the wave and MABL state parameters described in the prior section: (Fig. 10a) significant wave height H_s (m), (Fig. 10b) wind speed U_{10} (m s^{-1}), (Fig. 10c) first moment of the $\Lambda(c)$ distribution, and (Fig. 10d) computed dissipation by wave breaking F (W m^{-2}). The measured aerosol volumetric concentration appears better correlated with H_s ($r^2 = 0.71$). Note that the first moment of the $\Lambda(c)$ distributions is often used to estimate active whitecap coverage: see, for example, Kleiss and Melville (2010, 2011). The first moment of the $\Lambda(c)$ distributions ($r^2 = 0.54$), the spectral estimate of the energy dissipated by wave breaking F ($r^2 = 0.49$) and the wind speed U_{10} (in Fig. 10b; $r^2 = 0.48$), all show significantly lower correlations. This is of importance, as the wind speed has traditionally been used to parameterize sea spray source generation functions (de Leeuw et al. 2011; Veron 2015).

d. Scaling of aerosol volumetric concentration

To improve our understanding of the physical processes leading to the generation of such aerosol distributions in the MABL and to relate them to the mechanisms through which marine aerosols may be created, we conduct a classical dimensional analysis of the dependence of $\mathscr{V}$, the total aerosol volumetric concentration, on other variables and parameters that characterize the local atmospheric and wave states. Note that $\mathscr{V}$ is the ratio of the total volume of aerosol $\mathscr{V}_p$ divided by the total volume of air $\mathscr{V}_{\text{air}}$ and that $\mathscr{V} \equiv V$ for the measurements collected at $z = 30$ m in the present study.

The term $\mathscr{V}_p$ can be written as $f(H_s, u_*, \nu, \Gamma, g, \rho_a, \rho_w, k_p, \mathscr{V}_{\text{air}}, z)$, where ν is the kinematic viscosity of water; Γ is the surface tension; ρ_a and ρ_w are the density of air and water, respectively; and k_p is the wavenumber at the peak of the wave spectrum. Aerated breaking is expected over the wavenumber range bounded at its lower end by k_p up to the wavenumber at the minimum phase speed in the gravity wave range k_m, defined as

$$k_m = \sqrt{\frac{\rho_w g}{\Gamma}}. \qquad (17)$$

Through dimensional analysis, we obtain

$$\mathscr{V} = \frac{\mathscr{V}_p}{\mathscr{V}_{\rm air}} = f\left(\frac{u_* H_s}{\nu}, H_s k_p, \frac{c_p}{u_*}, \frac{\rho_a}{\rho_w}, \frac{k_m}{k_p}, B_o\right) q\left(\frac{z}{h_o}\right), \qquad (18)$$

where $u_* H_s/\nu$ is a wave-state-dependent Reynolds number, $H_s k_p$ is the significant wave slope, c_p/u_* is the wave age computed using the wavelength at the peak of the wave spectrum, B_o is the spectral Bond number that uses the speed attained in a ballistic trajectory from a height $H_s/2$ such that $B_o = (\rho_w - \rho_a)(gH_s)^2/g\Gamma$, and z/h_o is the ratio between the measurement height above mean sea level and the upper height of the evaporative region, set to H_s (see section 3a). The function f effectively represents the amplitude of the volumetric concentration $\mathscr{V}$, while q captures the dependence on z. Unfortunately, we cannot characterize q with the present dataset, where detailed measurements are only available at one measurement height: $z = 30$ m. Instead, we limit the scaling analysis to the amplitude term of $\mathscr{V}$ and f, using V, the volumetric concentration measured at 30 m, such that

$$V = f\left(\frac{u_* H_s}{\nu}, H_s k_p, \frac{c_p}{u_*}, \frac{\rho_a}{\rho_w}, \frac{k_m}{k_p}, B_o\right). \qquad (19)$$

That is, by definition $q(z/30) = 1$. We neglect here ρ_a/ρ_w, which is approximately constant in our measurements, and k_m/k_p, as $k_m \gg k_p$. Since the ratio $(\rho_w - \rho_a)/g\Gamma$ was approximately constant during the experiment, and the remaining term only depends on H_s, we are left with

$$V = f\left[\left(\frac{u_* H_s}{\nu}\right)^{\alpha} (H_s k_p)^{\beta} \left(\frac{c_p}{u_*}\right)^{\gamma}\right]. \qquad (20)$$

Without loss of generality we can set $\alpha = 1$, then β and γ are iteratively varied to minimize a square difference cost function of the total aerosol volumetric concentration V. We find the best collapse for $\beta = 0.1$ and $\gamma = 3/4$ corresponding to $r^2 = 0.77$. The nondimensional aerosol volumetric concentration for the HIRES experiment is shown in Fig. 11 as well as from GOTEX (Romero and Melville 2010a; Kleiss and Melville 2010, 2011), described in the appendix. Aerosol number distributions and wave and atmospheric parameters were computed for research flight 10 (RF10) of GOTEX, following the same procedures used for the HIRES experiment.

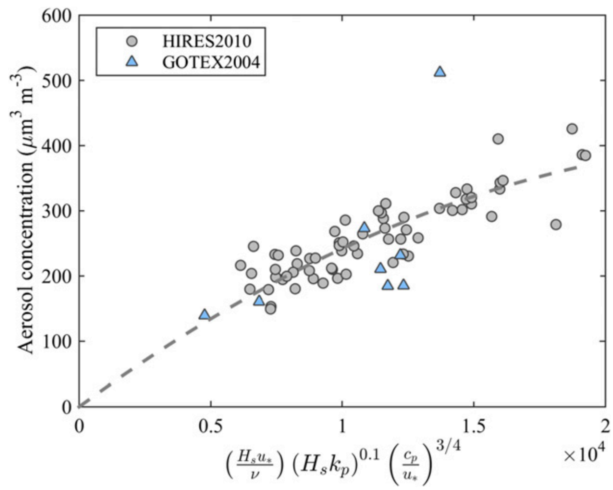

FIG. 11. Nondimensional total aerosol volumetric concentration for the HIRES and GOTEX2004 experiments plotted as a function of wave-state Reynolds number, significant wave slope, and wave age. The corresponding quadratic fit with the y intercept forced to zero is shown as a dashed gray line.

As the airborne aerosol sensors have a sample volume, the chance of undersampling, oversampling, or mischaracterizing the spatial variability of the aerosol distribution increases for the larger aerosols, in particular for diameters above 20 μm. In that context, a more conservative approach consists of minimizing the same cost function described above, but this time for aerosol particles of diameter d smaller than 20 μm.

Taking $\alpha = 1$, we find $\beta = 0.25$ and $\gamma = 1$ corresponding to a r^2 of 0.84. Figure 12 shows the corresponding nondimensional volumetric concentration, and two quadratic fits computed from the HIRES data (red: y intercept forced to zero, gray: no forcing). For aerosol diameters smaller than 20 μm, we find that the aerosol volumetric concentration can be parameterized by a wave Reynolds number, significant slope, and wave age such that

$$V = a\xi^2 + b\xi + c, \qquad (21)$$

where

$$\xi = \left(\frac{u_* H_s}{\nu}\right)(H_s k_p)^{0.25}\left(\frac{c_p}{u_*}\right). \qquad (22)$$

For the quadratic fits shown in Fig. 12, we find $a = -2.0 \times 10^{-7}$ (-2.36×10^{-7}), $b = 0.015$ (0.016), and $c = 14.7$ (0), with the values in the parentheses corresponding to the case with the y intercept forced to zero.

Relating the aerosol volumetric concentration to both atmospheric and wave-state variables over a wide range

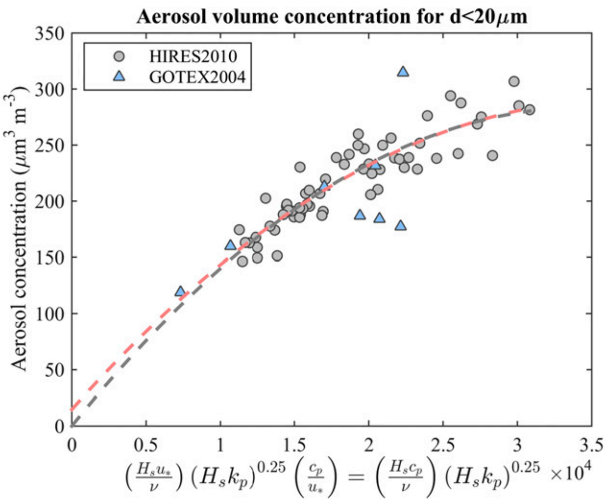

FIG. 12. Nondimensional aerosol volumetric concentration for the HIRES and GOTEX2004 experiments, plotted as a function of wave-state Reynolds number, significant wave slope, and wave age for aerosol diameters smaller than 20 μm. The corresponding quadratic fit with the y intercept forced to zero is shown as a dashed gray line, while the one without forcing is shown in light red color.

of environmental conditions is an important step toward better parameterization of the SSSGFs.

4. Summary

In this study, we have presented detailed measurements of aerosol number concentration in the marine atmospheric boundary layer at altitudes ranging from as low as 30 m and up to 800 m MSL over a broad range of environmental conditions (significant wave height H_s of 2 to 4.5 m and wind speed at 10-m height U_{10} of 10 to 18 m s^{-1}) collected from instrumented research aircraft during the HIRES and GOTEX experiments. The sea state (parameterized as significant wave height), moments of the breaker distribution $\Lambda(c)$, and wave breaking dissipation F were measured by a suite of electro-optical sensors that included the NASA ATM.

Large aerosol particles ($d > 40\mu$m) were found up to the top of the MABL. This is of importance as the role, generation, and transport mechanisms of this range of aerosols are poorly understood (Veron 2015) but are known to contribute to sensible and latent heat fluxes and can also offer a means of transport for larger organic carbon compounds from the ocean, including the dissolved oxygen component (DOC) and the particulate organic component (POC; see Quinn et al. 2015).

Though much progress has been made in the past two decades, our understanding of the physical processes that occur when aerosol particles are created and ejected into the airflow, especially for the larger particles with $d > 20\mu$m, is very limited. The scatter in SSSG estimates, especially for larger particles, is significant and has serious implications for modeling global aerosol budgets.

We presented here the sensitivity to a nondimensional parameterization of the aerosol volumetric concentration measured at 30 m MSL during the HIRES and GOTEX experiments. Though limited to one measurement height (30 m MSL) in the present work, this approach shows promise for including wave effects into models of marine aerosol production. More laboratory and field measurements are needed, perhaps along the

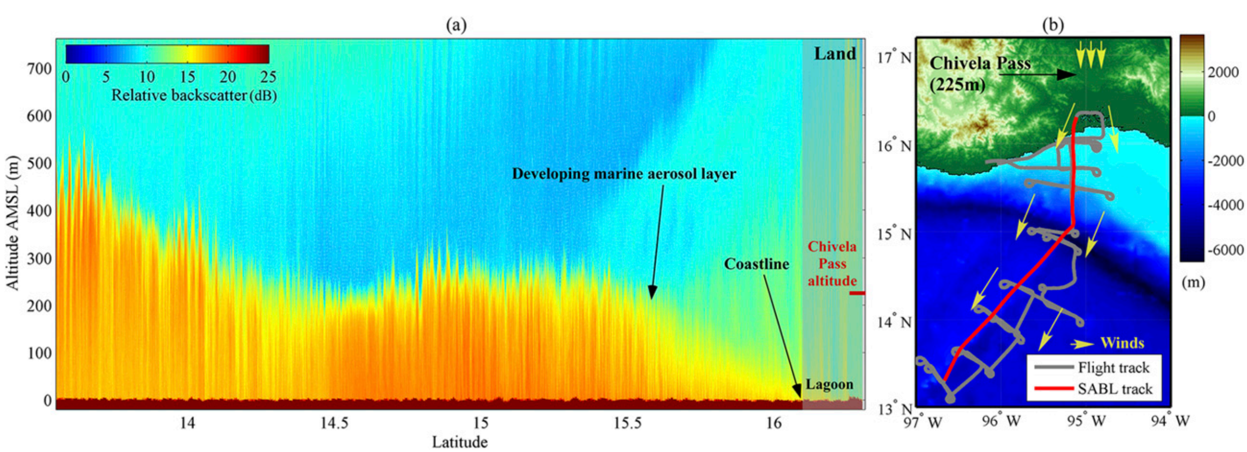

FIG. A1. (a) SABL lidar profiles (1064-nm wavelength) of range-corrected backscatter in dB during the return leg of RF10 during the GOTEX2004 experiment on 27 Feb 2004. The corresponding flight track is shown in red in the right plot. (b) Topographic map of the experiment operation area, showing the flight track on 27 Feb 2004 (RF10, gray solid line with the return track featured in red). The yellow arrows conceptually represent the wind direction during a Tehuano event and the location of the Chivela Pass. Note the developing height of the aerosol boundary layer offshore in the downwind (decreasing latitude) fetch, starting near the surface at the coastline, well below the altitude the Chivela Pass.

lines of the Reid et al. (2001) experiment, collecting direct aerosol flux measurement in a fetch-limited environment, both in the surface aerosol source layer, perhaps from a research vessel, buoy, or platform or unmanned surface vehicles (Lenain and Melville 2014), and at height, from an aircraft (manned or unmanned), collocated with detailed measurements of the wave kinematics and wave breaking.

Acknowledgments. We thank the pilots and scientific staff at CIRPAS, especially Haf Jonsson, for their support during flight operation and data postprocessing. We thank Bill Krabill and NASA for the loan of the ATM lidar and the support of the ATM operator team: James Yungel, Matt Linkswiler, and Earl Frederick. We are thankful to Fabrice Veron for providing useful suggestions at an early stage of this work. We thank two anonymous reviewers and the editor Dr. Ilker Fer for their suggestions, which improved the paper. This project was supported by grants to WKM from the Physical Oceanography programs at ONR (N00014-08-1-0499, N00014-02-1-0249, and N00014-14-1-0710) and NSF (OCE-1155403).

APPENDIX

The Gulf of Tehuentepec Experiment (GOTEX 2004)

The GOTEX experiment was undertaken in February 2004, in the Gulf of Tehuantepec off the Pacific coast of Mexico, an area known for predictable and repeatable offshore wind jets (known as Tehuano) during the wintertime. As cold weather systems move south into the Gulf of Mexico, east of the Sierra Madre, an atmospheric pressure difference across the Tehuentepec isthmus creates strong, offshore westerly winds flowing through a gap in the mountain range, the Chivela Pass (225 m MSL).

The primary goal of GOTEX was to characterize the evolution of the directional wave spectrum, wave breaking, and surface kinematics in the fetch-limited wave environment generated during Tehuano wind events. An aircraft, the NSF–NCAR C-130Q *Hercules*, was instrumented with a suite of electro-optical systems that included an earlier version of the NASA ATM lidar [see Romero and Melville (2010a) and Kleiss and Melville (2010, 2011) for details]. Atmospheric momentum flux and surface wave measurements were taken from Romero and Melville (2010a) in the present analysis.

Aerosol measurements were made using a suite of sensors, similar to the CIRPAS *Twin Otter* setup, installed on wing pylons to provide in situ sampling of the particles present in the airflow. Among a large suite of atmospheric, cloud physics, and chemistry sensors, PMS PCASP-100X and PMS FSSP-100 measured particle size (diameter) from 0.001 to 2.11 μm and 1 to 53.45 μm, respectively, over 30 size bins for each system. The Earth Observing Laboratory Scanning Aerosol Backscatter Lidar (EOL SABL), a compact upward/downward-looking aerosol lidar, was also installed on the aircraft. This lidar, operating in the IR (1064 nm) and green (532 nm) wavelengths, was designed to provide qualitative information on the structure of the atmosphere.

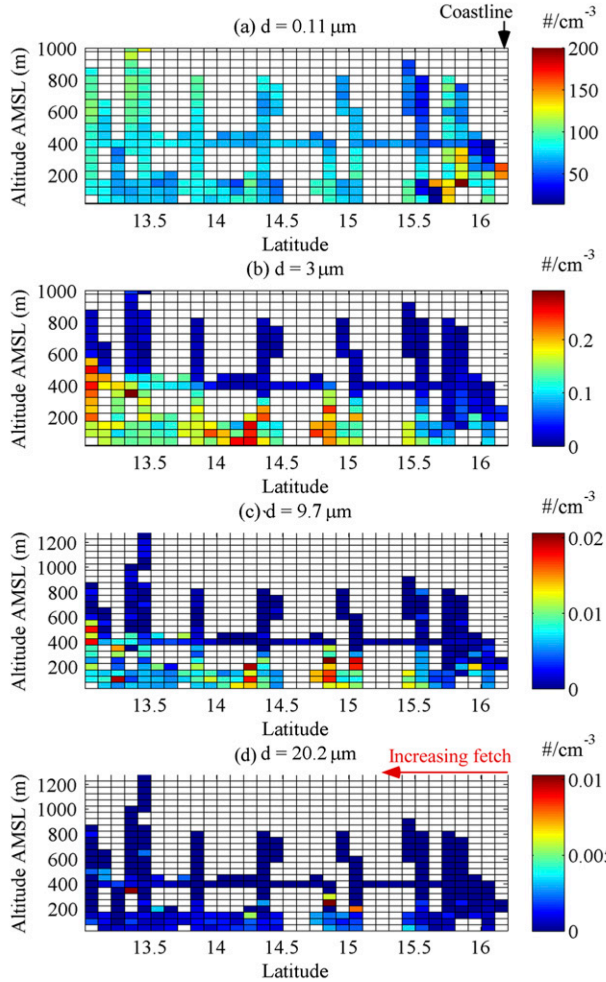

FIG. A2. Aerosol concentration measured during the 30 m MSL portions of RF10 on 27 Feb 2004 for four aerosol diameters: (a) 0.11, (b) 3, (c) 9.7, and (d) 20.2 μm.

Figure A1a shows the SABL lidar profiles (1064-nm wavelength) of range-corrected backscatter in units of decibels during the return leg of RF10 during the GOTEX2004 experiment on 27 February 2004. The corresponding flight track is shown in red in Fig. A1b. Only the 1064-nm data are shown, as the 532-nm data exhibit similar results. The SABL lidar image shows the development of the aerosol boundary layer offshore in the downwind (decreasing latitude) increasing fetch, starting near the surface at the coastline, well below the altitude of the Chivela Pass, also shown in the same figure. The height of the aerosol boundary layer rapidly increases from the coastline up to 15.5° latitude, reaching close to 300 m MSL and then remains approximately constant up to 14.5° latitude, where the height of the aerosol layer starts increasing again, reaching 500 m MSL at 13.5° latitude. Though low lidar backscatter levels north of 16° latitude are likely associated with small diameter aerosols generated on land, they remain much less than the backscatter shown offshore in the marine aerosol layer. This is confirmed in Fig. A2, where the in situ aerosol concentration measured from the sensors installed on the C130 wing pylons is shown as a function of latitude and height MSL for four aerosol sizes: 0.11, 3, 9.7, and 20.2 μm. The development of the aerosol boundary layer is evident, especially for the particles of diameter 3–10 μm, with increasing height downwind (decreasing latitude), consistent with the SABL qualitative picture. The smaller diameter particles (0.11 μm) do not show the same spatial pattern, likely driven by aerosol from land or a nonlocal source, especially at height. Low concentrations of larger diameter aerosols are present, mostly limited to the lowest part of the aerosol boundary layer. Detailed analysis of this dataset is currently underway and will be the topic of a separate publication.

REFERENCES

Andreas, E. L, 1995: The temperature of evaporating sea spray droplets. *J. Atmos. Sci.*, **52**, 852–862, doi:10.1175/1520-0469(1995)052<0852:TTOESS>2.0.CO;2.

Banner, M. L., and W. L. Peirson, 2007: Wave breaking onset and strength for two-dimensional deep-water wave groups. *J. Fluid. Mech.*, **585**, 93–115, doi:10.1017/S0022112007006568.

Brown, E. D., J. H. Churnside, R. L. Collins, T. Veenstra, J. J. Wilson, and K. Abnett, 2002: Remote sensing of capelin and other biological features in the North Pacific using lidar and video technology. *ICES J. Mar. Sci.*, **59**, 1120–1130, doi:10.1006/jmsc.2002.1282.

Carrera, P., J. Churnside, G. Boyra, V. Marques, C. Scalabrin, and A. Uriarte, 2006: Comparison of airborne lidar with echosounders: A case study in the coastal Atlantic waters of southern Europe. *ICES J. Mar. Sci.*, **63**, 1736–1750, doi:10.1016/j.icesjms.2006.07.004.

Churnside, J. H., V. V. Tatarskii, and J. J. Wilson, 1998: Oceanographic lidar attenuation coefficients and signal fluctuations measured from a ship in the Southern California Bight. *Appl. Opt.*, **37**, 3105–3112, doi:10.1364/AO.37.003105.

——, J. J. Wilson, and V. V. Tatarskii, 2001: Airborne lidar for fisheries applications. *Opt. Eng.*, **40**, 406–414, doi:10.1117/1.1348000.

Cunningham, E., 1910: On the velocity of steady fall of spherical particles through fluid medium. *Proc. Roy. Soc. London*, **A83**, 357–365, doi:10.1098/rspa.1910.0024.

de Leeuw, G., E. L Andreas, M. D. Anguelova, C. Fairall, E. R. Lewis, C. O'Dowd, M. Schulz, and S. E. Schwartz, 2011: Production flux of sea spray aerosol. *Rev. Geophys.*, **49**, RG2001, doi:10.1029/2010RG000349.

Drazen, D. A., W. K. Melville, and L. Lenain, 2008: Inertial scaling of dissipation in unsteady breaking waves. *J. Fluid Mech.*, **611**, 307–332, doi:10.1017/S0022112008002826.

Duncan, J., 1981: An experimental investigation of breaking waves produced by a towed hydrofoil. *Proc. Roy. Soc. London*, **A377**, 331–348, doi:10.1098/rspa.1981.0127.

Fairall, C., J. Kepert, and G. Holland, 1994: The effect of sea spray on surface energy transports over the ocean. *Global Atmos. Ocean Syst.*, **2**, 121–142.

——, E. F. Bradley, J. Hare, A. Grachev, and J. Edson, 2003: Bulk parameterization of air–sea fluxes: Updates and verification for the COARE algorithm. *J. Climate*, **16**, 571–591, doi:10.1175/1520-0442(2003)016<0571:BPOASF>2.0.CO;2.

——, M. Banner, W. Peirson, W. Asher, and R. Morison, 2009: Investigation of the physical scaling of sea spray spume droplet production. *J. Geophys. Res.*, **114**, C10001, doi:10.1029/2008JC004918.

Grare, L., L. Lenain, and W. K. Melville, 2013: Wave-coherent airflow and critical layers over ocean waves. *J. Phys. Oceanogr.*, **43**, 2156–2172, doi:10.1175/JPO-D-13-056.1.

Hanley, K. E., S. E. Belcher, and P. P. Sullivan, 2010: A global climatology of wind-wave interaction. *J. Phys. Oceanogr.*, **40**, 1263–1282, doi:10.1175/2010JPO4377.1.

Hwang, P. A., D. W. Wang, E. J. Walsh, W. B. Krabill, and R. N. Swift, 2000a: Airborne measurements of the wavenumber spectra of ocean surface waves. Part I: Spectral slope and dimensionless spectral coefficient. *J. Phys. Oceanogr.*, **30**, 2753–2767, doi:10.1175/1520-0485(2001)031<2753:AMOTWS>2.0.CO;2.

——, ——, ——, ——, and ——, 2000b: Airborne measurements of the wavenumber spectra of ocean surface waves. Part II: Directional distribution. *J. Phys. Oceanogr.*, **30**, 2768–2787, doi:10.1175/1520-0485(2001)031<2768:AMOTWS>2.0.CO;2.

Jones, K. F., and E. L Andreas, 2012: Sea spray concentrations and the icing of fixed offshore structures. *Quart. J. Roy. Meteor. Soc.*, **138**, 131–144, doi:10.1002/qj.897.

Kleiss, J. M., and W. K. Melville, 2010: Observations of wave breaking kinematics in fetch-limited seas. *J. Phys. Oceanogr.*, **40**, 2575–2604, doi:10.1175/2010JPO4383.1.

——, and ——, 2011: The analysis of sea surface imagery for whitecap kinematics. *J. Atmos. Oceanic Technol.*, **28**, 219–243, doi:10.1175/2010JTECHO744.1.

Krabill, W., R. Thomas, K. Jezek, K. Kuivinen, and S. Manizade, 1995: Greenland Ice Sheet thickness changes measured by laser altimetry. *Geophys. Res. Lett.*, **22**, 2341–2344, doi:10.1029/95GL02069.

Lenain, L., and W. K. Melville, 2014: Autonomous surface vehicle measurements of the oceans response to Tropical Cyclone Freda. *J. Atmos. Oceanic Technol.*, **31**, 2169–2190, doi:10.1175/JTECH-D-14-00012.1.

Lewis, E. R., and S. E. Schwartz, 2004: *Sea Salt Aerosol Production: Mechanisms, Methods, Measurements, and Models—A Critical Review*. Geophys. Monogr., Vol. 152, Amer. Geophys. Union, 413 pp.

Mårtensson, E., E. Nilsson, G. de Leeuw, L. Cohen, and H.-C. Hansson, 2003: Laboratory simulations and parameterization of the primary marine aerosol production. *J. Geophys. Res.*, **108**, 4297, doi:10.1029/2002JD002263.

Melville, W. K., 1994: Energy dissipation by breaking waves. *J. Phys. Oceanogr.*, **24**, 2041–2049, doi:10.1175/1520-0485(1994)024<2041:EDBBW>2.0.CO;2.

Monahan, E. C., D. E. Spiel, and K. L. Davidson, 1986: A model of marine aerosol generation via whitecaps and wave disruption. *Oceanic Whitecaps*, Oceanographic Sciences Library Series, Vol. 2, Springer, 167–174.

Mueller, J. A., and F. Veron, 2009: A sea state-dependent spume generation function. *J. Phys. Oceanogr.*, **39**, 2363–2372, doi:10.1175/2009JPO4113.1.

Norris, S. J., I. Brooks, B. Moat, M. Yelland, G. de Leeuw, R. Pascal, and B. Brooks, 2013a: Near-surface measurements of sea spray aerosol production over whitecaps in the open ocean. *Ocean Sci.*, **9**, 133–145, doi:10.5194/os-9-133-2013.

——, ——, and D. J. Salisbury, 2013b: A wave roughness Reynolds number parameterization of the sea spray source flux. *Geophys. Res. Lett.*, **40**, 4415–4419, doi:10.1002/grl.50795.

Oost, W., G. Komen, C. Jacobs, and C. Van Oort, 2002: New evidence for a relation between wind stress and wave age from measurements during ASGAMAGE. *Bound.-Layer Meteor.*, **103**, 409–438, doi:10.1023/A:1014913624535.

Ovadnevaite, J., A. Manders, G. De Leeuw, D. Ceburnis, C. Monahan, A.-I. Partanen, H. Korhonen, and C. O'Dowd, 2014: A sea spray aerosol flux parameterization encapsulating wave state. *Atmos. Chem. Phys.*, **14**, 1837–1852, doi:10.5194/acp-14-1837-2014.

Phillips, O., 1985: Spectral and statistical properties of the equilibrium range in wind-generated gravity waves. *J. Fluid Mech.*, **156**, 505–531, doi:10.1017/S0022112085002221.

Pizzo, N., and W. K. Melville, 2013: Vortex generation by deep-water breaking waves. *J. Fluid Mech.*, **734**, 198–218, doi:10.1017/jfm.2013.453.

Quinn, P. K., D. B. Collins, V. H. Grassian, K. A. Prather, and T. S. Bates, 2015: Chemistry and related properties of freshly emitted sea spray aerosol. *Chem. Rev.*, **115**, 4383–4399, doi:10.1021/cr500713g.

Reid, J. S., H. H. Jonsson, M. H. Smith, and A. Smirnov, 2001: Evolution of the vertical profile and flux of large sea-salt particles in a coastal zone. *J. Geophys. Res.*, **106**, 12 039–12 053, doi:10.1029/2000JD900848.

——, and Coauthors, 2007: An assessment of the meteorological conditions leading to the NOAA WP-3D engine compressor stalls of February 9, 2007, due to sea salt aerosol particle fouling. Naval Research Laboratory Memo. Rep. NRL/MR/7540–07-9080, 39 pp.

Romero, L., and W. K. Melville, 2010a: Airborne observations of fetch-limited waves in the Gulf of Tehuantepec. *J. Phys. Oceanogr.*, **40**, 441–465, doi:10.1175/2009JPO4127.1.

——, and ——, 2010b: Numerical modeling of fetch-limited waves in the Gulf of Tehuantepec. *J. Phys. Oceanogr.*, **40**, 466–486, doi:10.1175/2009JPO4128.1.

——, ——, and J. M. Kleiss, 2012: Spectral energy dissipation due to surface wave breaking. *J. Phys. Oceanogr.*, **42**, 1421–1444, doi:10.1175/JPO-D-11-072.1.

Rouault, M. P., P. G. Mestayer, and R. Schiestel, 1991: A model of evaporating spray droplet dispersion. *J. Geophys. Res.*, **96**, 7181–7200, doi:10.1029/90JC02569.

Shpund, J., M. Pinsky, and A. Khain, 2011: Microphysical structure of the marine boundary layer under strong wind and spray formation as seen from simulations using a 2D explicit microphysical model. Part I: The impact of large eddies. *J. Atmos. Sci.*, **68**, 2366–2384, doi:10.1175/2011JAS3652.1.

——, J. Zhang, M. Pinsky, and A. Khain, 2012: Microphysical structure of the marine boundary layer under strong wind and spray formation as seen from simulations using a 2D explicit microphysical model. Part II: The role of sea spray. *J. Atmos. Sci.*, **69**, 3501–3514, doi:10.1175/JAS-D-11-0281.1.

——, ——, ——, and ——, 2014: Microphysical structure of the marine boundary layer under strong wind and sea spray formation as seen from a 2D explicit microphysical model. Part III: Parameterization of height-dependent droplet size distribution. *J. Atmos. Sci.*, **71**, 1914–1934, doi:10.1175/JAS-D-12-0201.1.

Smith, M., P. Park, and I. Consterdine, 1993: Marine aerosol concentrations and estimated fluxes over the sea. *Quart. J. Roy. Meteor. Soc.*, **119**, 809–824, doi:10.1002/qj.49711951211.

Sutherland, P., and W. K. Melville, 2013: Field measurements and scaling of ocean surface wave-breaking statistics. *Geophys. Res. Lett.*, **40**, 3074–3079, doi:10.1002/grl.50584.

Terrill, E., and W. K. Melville, 1997: Sound-speed measurements in the surface-wave layer. *J. Acoust. Soc. Amer.*, **102**, 2607–2625, doi:10.1121/1.420315.

Toffoli, A., A. Babanin, M. Donelan, B. Haus, and D. Jeong, 2011: Estimating sea spray volume with a laser altimeter. *J. Atmos. Oceanic Technol.*, **28**, 1177–1183, doi:10.1175/2011JTECHO827.1.

Veron, F., 2015: Ocean spray. *Annu. Rev. Fluid Mech.*, **47**, 507–538, doi:10.1146/annurev-fluid-010814-014651.

——, C. Hopkins, E. Harrison, and J. Mueller, 2012: Sea spray spume droplet production in high wind speeds. *Geophys. Res. Lett.*, **39**, L16602, doi:10.1029/2012GL052603.

Zhao, D., and Y. Toba, 2001: Dependence of whitecap coverage on wind and wind-wave properties. *J. Oceanogr.*, **57**, 603–616, doi:10.1023/A:1021215904955.

——, ——, K.-I. Sugioka, and S. Komori, 2006: New sea spray generation function for spume droplets. *J. Geophys. Res.*, **111**, C02007, doi:10.1029/2005JC002960.